Sensitivity of the Time-Shift Technique in Characterizing Non-spherical Drops

Li,Lingxi[1*]; Rosenkranz, Simon[2]; Schäfer, Walter[2]; Tropea, Cameron[1]
1: Institute of Fluid Mechanics and Aerodynamics, Technische Universität Darmstadt, Alarich-Weiss-Strasse 10, 64287 Darmstadt, Germany
2: AOM-Systems GmbH, Flughafenstrasse 15, 64347 Griesheim, Germany
* Correspondent author: li@sla.tu-darmstadt.de

Keywords: Light scattering, Gaussian beam, non-spherical drop, time-shift technique

1. Introduction

This study focuses on the measurement of non-spherical drops using the time-shift technique. Non-spherical drops arise in many applications, but are generally more predominant with larger drops, since surface tension insures that small drops rapidly become and remain spherical. Difficulties arise in optically measuring the size of non-spherical drops, whereby the measurement error depends strongly on the measurement principle and measurement technique used. Reviews of available optical techniques for drop/spray characterization are available [3], [6]; however, the issue of non-sphericity has seldom been comprehensively or systematically investigated for any single technique. For certain techniques, in particular the phase Doppler technique, the influence of non-sphericity has been qualitatively characterized for certain drop alignments [7], [17], and optical configurations have been devised to recognize drop non-sphericity, eliminating these values from further statistical analysis, because of the resulting erroneous size measurement [4]. This approach is typically known as 'sphericity validation'. While direct drop imaging detects non-sphericity, it has the obvious disadvantage of only capturing the projection of drops onto an imaging plane, which for non-spherical drops may also yield erroneous size estimates. The difficulty with eliminating non-spherical drops from statistical ensembles is that especially the large drops often make up a large fraction of the spray mass/volume, which in many applications is the most desired quantity, i.e. the local volume/mass flux density. Thus, any method to measure the size of non-spherical drops is welcome, if the expected accuracy can also be estimated.

The present contribution addresses the issue of non-sphericity in drop sizing using the time-shift technique. The reason for concentrating on the time-shift technique is that there is reasonable grounds to assume that the time-shift technique will exhibit lower errors when measuring non-spherical drops than other optical techniques. The time-shift technique uses a highly focused Gaussian beam to separate different scattering orders during passage of a drop/particle through the beam, typically detecting light in the near backscatter direction. Comprehensive descriptions

of this technique can be found in [11], [17], [20], and these will not be repeated in the present contribution.

One of the complicating factors when examining response of optical techniques to drop non-sphericity is that compared to spherical drops, now also the orientation of the drop with respect to the optical axis and detector must be considered. In any case, to examine sensitivity and response of optical techniques to non-sphericity, one pre-requisite is to compute light scattered from non-spherical drops. This has been achieved analytically and numerically for numerous special cases and with definite measurement techniques in mind [9], [13], [14], [15]; however, most approaches rapidly reach computational unfeasible limits for larger drops, exactly the ones that are to be expected to be non-spherical. For this reason, the method of choice in the present study is to use ray tracing, i.e. geometrical optics. The condition for this geometrical optics is valid is that the drop is significantly larger than the wavelength of the light being used.

The next section describes the computational approach, including validation by comparison to analytic solutions. A section follows in which the signal generation of the time-shift technique is simulated, whereby the response and sensitivity of the technique to non-sphericity will be quantified. The final section summarizes the measurement accuracy of certain statistical quantities when measuring sprays containing non-spherical drops.

2. Computational Procedure

2.1. Description of the laser beam

When describing the laser beam incident on the drop, characteristics typical of a time-shift instrument have been used, for instance the SpraySpy instrument from AOM-Systems [1]. In this case, the laser beam has a beam waist of 1 mm in the X direction and 10 µm in the Y direction, the Z direction being the direction of laser beam propagation. Such a non-circular Gaussian beam (light sheet) is used to improve the directional sensitivity of the instrument, as described in [20]. This non-circular Gaussian beam is treated as a bundle of rays, each ray being defined by its starting point, propagation direction, and the initial amplitude of the electric field E_0. The starting points of the large number of beams used in the simulation are randomly distributed in space. This is similar to the approach used in [18] and experience confirms that convergence of the computed light scattering diagrams is achieved with much fewer rays than if a regular grid spacing is used for the starting points. Fig. 1 illustrates exemplarily the starting points of such a beam, showing the transverse plane of rays for the focused non-circular Gaussian beam.

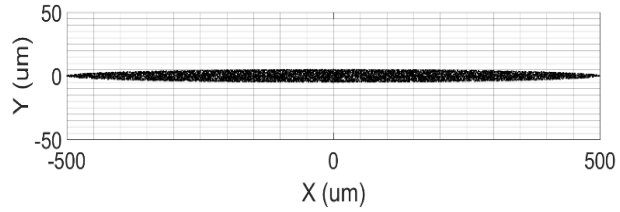

Fig. 1: Randomly generated starting points for the ray tracing

For a non-circular Gaussian laser beam, the complex amplitude can be described as [19]:

$$E(\boldsymbol{r}, z) = E_0(z)\, exp\left[-i\phi_{ac} + i\eta(z) - ik\left(\frac{x^2}{2q_1(z)} + \frac{y^2}{2q_2(z)}\right)\right] \quad (1)$$

Where the ϕ_{ac} is the phase accumulated from the chosen reference point. r is the transversal vector, which is a function of (x, y); the Gouy phase $\eta(z)$ is the average of the two phase of symmetry, and the q parameter could be obtained from the following equation [16]:

$$\frac{1}{q_n(z)} = \frac{1}{R(z)} - i\frac{\lambda}{\pi\omega_n^2(z)}, n = 1,2 \quad (2)$$

where w_i is the principle semi-axes of the elliptical beam and R(z) is the principle radii of curvature of the wavefront. The Gouy phase is given by [2]

$$\eta(z) = \frac{1}{2}\left[tan^{-1}\left(\frac{z - z_{01}}{z_{R1}}\right) + tan^{-1}\left(\frac{z - z_{02}}{z_{R2}}\right)\right] \quad (3)$$

where z_{01} is the position of beam waist in Z direction and Z_{R1} is the Rayleigh Range.

In the time-shift signal different scattering orders are separated in time, so interference will not be considered. Hence, it is not necessary to follow the phase of each ray; however, the polarization must be accounted for, since the polarization influences the beam transmission at each interface (Fresnel equations[8]). Since the size of the drop is much smaller than the beam waist in the X direction, the amplitude of the rays which are incident on the drop are treated as constant in the X direction.

2.2. Description of the arbitrary spheroid in space

The primary coordinate system is centered at the beam waist and aligned such that the Z-axis is in the beam propagation direction; polarization is with respect to the X-axis (s polarization). The drop is a spheroid (ellipsoid of revolution), given by:

$$\frac{(x - x_0)^2}{a^2} + \frac{(y - y_0)^2}{b^2} + \frac{(z - z_0)^2}{c^2} = 1 \quad (4)$$

Where (x_0, y_0, z_0) are the coordinates of the drop with respect to the center of the Gaussian beam waist. However, in the present study the drop can also be arbitrarily orientated when passing through the laser beam. The particle rotation is achieved using the Euler rotation theorem, by which the rotation can be described using three angles. There are several variations of this matrix and the so-called ZXZ rotation is used in this study. A right-handed coordinate system with a

positive angle to represent any right-handed rotation is used. Rotations are first performed around the Z-axis through an angle Ψ, then around the (rotated) X'-axis of the body through an angle β, and finally around the Z'-axis of the body through an angle a. After performing the rotations, the entire body is translated. The body rotation of the spheroid is depicted in Fig. 2.

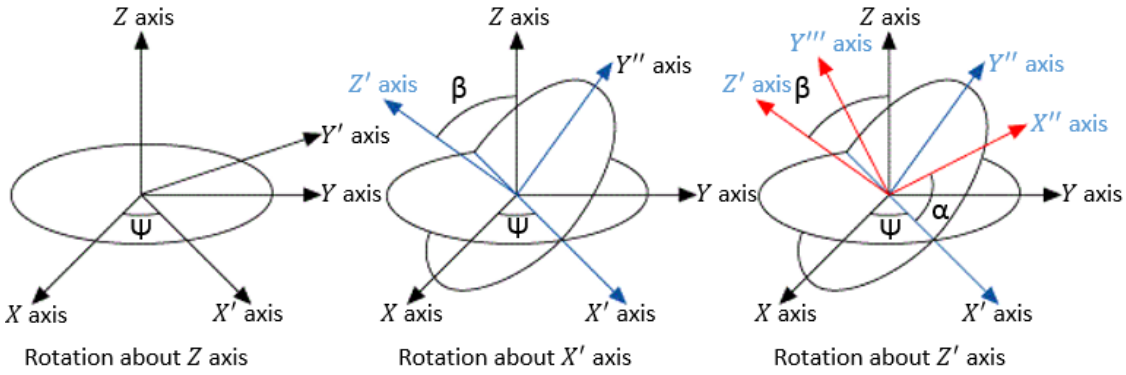

Fig. 2: Orientation of droplet after the ZXZ rotation.

If (x', y', z') are the coordinates of a particular point prior to rotation and translation, and (x, y, z) are the coordinates of the point after rotation and translation, then the following relations hold:

$$\begin{pmatrix} x' \\ y' \\ z' \end{pmatrix} = R_z(-\alpha)R_x(-\beta)R_z(-\Psi)\begin{pmatrix} x - x0 \\ y - z0 \\ z - z0 \end{pmatrix} \tag{5}$$

where:

$$R_z(\Psi) = \begin{pmatrix} cos\,\Psi & -sin\,\Psi & 0 \\ sin\,\Psi & cos\,\Psi & 0 \\ 0 & 0 & 1 \end{pmatrix} \tag{6}$$

$$R_x(\beta) = \begin{pmatrix} 1 & 0 & 0 \\ 0 & cos\,\beta & -sin\,\beta \\ 0 & sin\,\beta & cos\,\beta \end{pmatrix} \tag{7}$$

$$R_z(\alpha) = \begin{pmatrix} cos\,\alpha & -sin\,\alpha & 0 \\ sin\,\alpha & cos\,\alpha & 0 \\ 0 & 0 & 1 \end{pmatrix} \tag{8}$$

Substituting Eq. (5) in the Eq. (4), then the spheroid in space is given by:

$$\frac{[(cos\,\alpha\,cos\,\Psi - sin\,\alpha\,cos\,\beta\,sin\,\Psi)(x - x_0) + (-cos\,\alpha\,sin\,\Psi - sin\,\alpha\,cos\,\beta\,cos\,\Psi)(y - y_0) + sin\,\alpha\,sin\,\beta\,(z - z_0)]^2}{a^2} +$$
$$\frac{[(sin\,\alpha\,sin\,\Psi + cos\,\alpha\,cos\,\beta\,sin\,\Psi)(x - x_0) + (-sin\,\alpha\,sin\,\Psi + cos\,\alpha\,cos\,\beta\,cos\,\Psi)(y - y_0) - cos\,\alpha\,sin\,\beta\,(z - z_0)]^2}{b^2} +$$
$$\frac{[(sin\,\beta\,sin\,\Psi)(x - x_0) + (sin\,\beta\,cos\,\Psi)(y - y_0) + cos\,\beta\,(z - z_0)]^2}{c^2} = 1 \tag{9}$$

2.3. Ray tracing algorithm and validation

The ray tracing algorithm first checks whether a given ray intersects the drop and if so, the intersection point on the drop surface is calculated. The direction of the reflected ray and refracted ray at each interface intersection is computed using Snell's law and the amplitude of

the electric field is given by the Fresnel equations for the reflected and refracted (transmitted) rays [8]. For each ray, the computation for one scattering order is followed by the computation for the next scattering order, based on the computational results up to that stage. This process is repeated until the computation for a specified number of scattering orders of all rays is complete. The information of all rays is saved. To compute a scattering diagram, a point detector, defined using a solid scattering angle of 0.0029 sr, is traced through 0 to 180°. At each position the intensity of the scattered light (Eq. (10)) is given as the sum over the intensity of all rays falling onto the detector (Eq.(11)).

$$I_k = \frac{c}{2}|\boldsymbol{E}|^2 \tag{10}$$

$$I_{total}(\theta_i, \varphi_j) = \sum_{k=1}^{n} I_k \tag{11}$$

To validate the code, simulation results for a plane wave have been compared with the known Lorenz-Mie solution [10] for a transparent drop of relative refractive index m. As an example result, Fig. *3* illustrates the scattering diagram of the first five scattering orders for a 100µm drop, compared with the results from a Lorenz-Mie computation, invoking also a Debye series decomposition [5] to examine the agreement between individual scattering orders. The agreement is good, exhibiting the expected deviations arising from the geometric optics approach of ray tracing: the interference phenomena in the rainbows are not captured and neither is the effect of surface waves, evident especially in the scattering of first-order refraction at angles beyond about 85 degrees. Diffraction in forward scatter is not included in the ray tracing algorithm. Nevertheless, the ray tracing exhibits very good agreement for the first three scattering orders and is suitable for analyzing the signal generation of the time-shift technique.

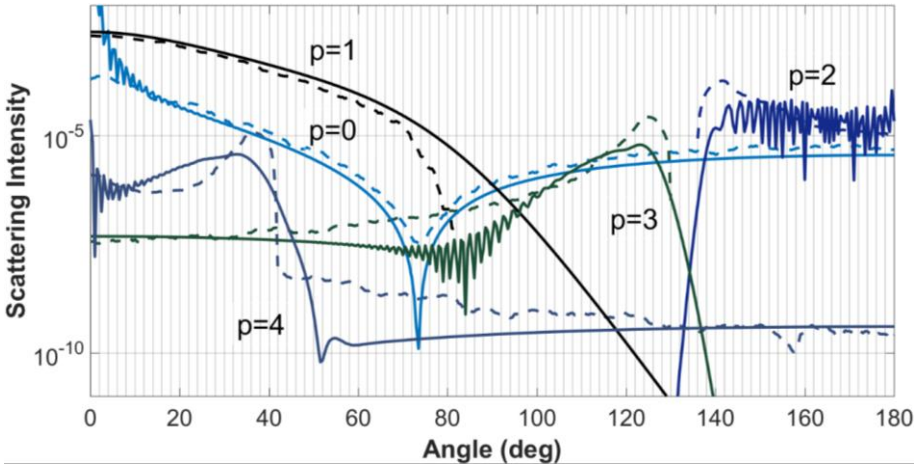

Fig. 3: Comparison between Lorenz-Mie theory with Debye series decomposition (solid lines) and ray tracing (dashed lines): drop diameter d=100µm, n_t=1.343

3. The time-shift technique and signal generation

The time-shift technique, also known as the pulsed-displacement technique, is a method to measure size, velocity, and relative refractive index (m) of spherical particles. As Figure 4 illustrates, a detector placed in the backscatter direction (e.g. 150°) will register a time dependent signal comprising several peaks, corresponding to the different scattering orders as a transparent drop passes through a shaped beam. Details about the measurement principle and optical design can be found in [20].

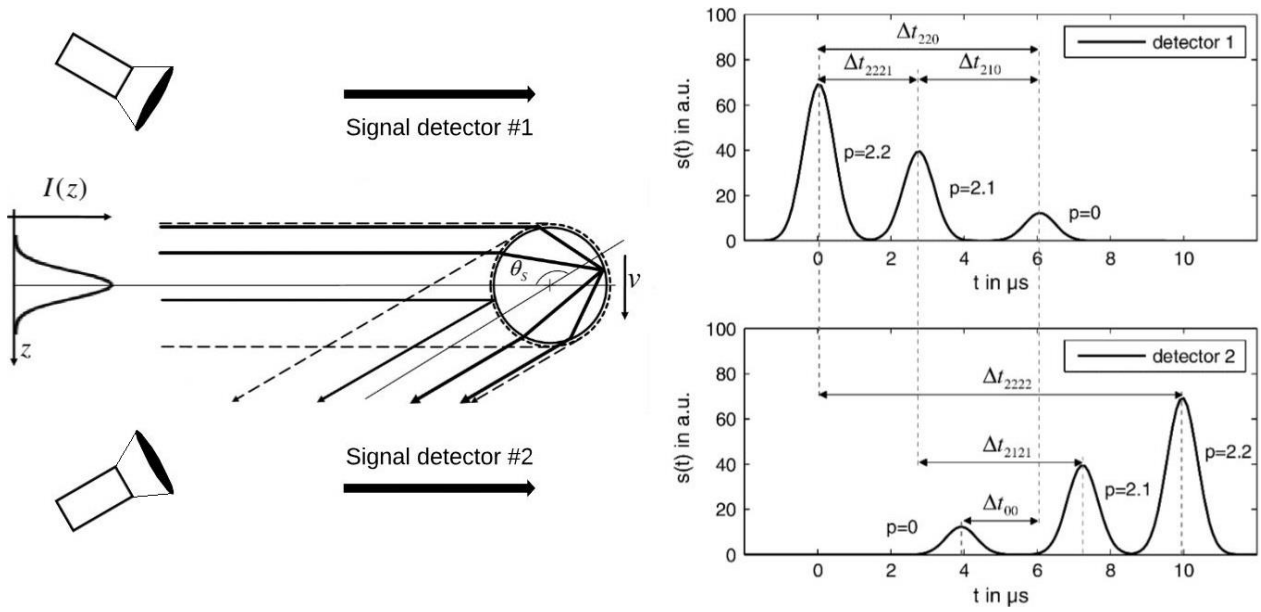

Figure 4: Principle of time-shift measurement technique [20]. p designates the scattering order, according to how many paths occur internal to the drop [20]. θ_s expresses the angle of the incident point for each scattering order.

To compute the signal arising from the passage of a drop through the focused beam of a time-shift instrument, first a drop position is specified and the light scattered onto a defined detector (position and size) is computed. With a given velocity, the drop is then displaced in flight direction by a step time of Δt and the computation is repeated. The intensity collected on the detector of diameter d for each drop position is converted into a time signal using the prescribed drop velocity v_z. To obtain the time-shift signal, the light scattering of all drop positions in which incident rays intersect with the drop need to be computed. The time-shift signal, illustrated in Figure 4 for detectors placed on either side of the illuminated laser sheet, comprises three main peaks; one arising from reflected light (p=0) and one each from the two modes of second-order refraction (p=2.1, p=2.2).

To understand the signal generation from an ellipsoidal droplet, the incident and exit angle ranges through which a ray passes to fall onto a prescribed detector is analyzed for reflected and

second-order refracted light. These angle ranges will be used to interpret the loss or overlap of signal peaks in the following section.

For reflection, the incident and glare points on the surface of the drop are coincident. The glare region which a finite size detector sees on the drop is computed by traversing a point detector over the real detector area. The point detector has the coordinate $(0, \ y_{d,} \ z_d)$. Figure 5a illustrates the ray path when a reflected ray is incident on the point detector.

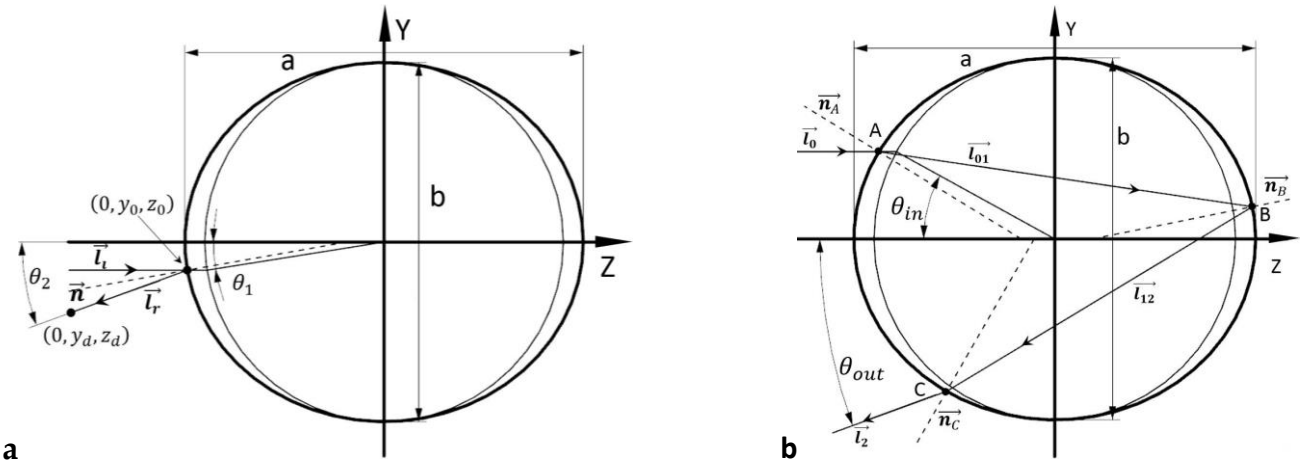

Figure 5: Ray paths for a point detector: a) reflection; b) second-order refraction

To reach the point detector Eq. (12) should be satisfied, where $\vec{l_i}$ and $\vec{l_r}$ represent the incident and the reflected ray vectors, and $\vec{n}$ is the normal vector at the incident/glare point $(0, \ y_0, \ z_0)$ and can be calculated as $\nabla f(0 \quad y_0 \quad z_0)/|f|$; where f is surface of the ellipsoid.

$$\frac{\left|\vec{l_i} \cdot \vec{n}\right|}{\left\|\vec{l_i}\right\| * \|\vec{n}\|} = \frac{\left|\vec{l_r} \cdot \vec{n}\right|}{\left\|\vec{l_r}\right\| * \|\vec{n}\|} \tag{12}$$

Substituting expressions for each of the variables in equation (12) yields the following relations:

$$|-\eta * cos\,\theta_1| = \left|\frac{-sin\,\theta_1 * (y_d + \eta * b * sin\,\theta_1) - \eta * cos\,\theta_1 * (z_d + a * cos\,\theta_1)}{\sqrt{(y_d + \eta * b * sin\,\theta_1)^2 + (z_d + a * cos\,\theta_1)^2}}\right| \tag{13}$$

Where, η is the aspect ratio $\eta = b/a$. This equation can be solved for the eccentric anomaly angle θ_1 , the angle correspondent to the incident/glare point.

To compute the glare point region for scattering by second-order refraction, the relationship between the angle incident θ_{in} and exit θ_{out} angles, illustrated in Figure 5b, has been computed by using the Eqs. (14) - (19) [12]:

$$L_{01} = \frac{1}{m}[L_0 - (L_0 \cdot n_A)n_A] - \sqrt{1 - \frac{1}{m^2} + \frac{1}{m^2}(L_0 \cdot n_A)^2} \cdot n_A \tag{14}$$

$$M_2 = \frac{\frac{y_0}{b^2} + \frac{p_0}{n_0}\frac{z_0}{c^2}}{\frac{1}{b^2} + \frac{p_0^2}{n_0^2}\frac{1}{c^2}} \tag{15}$$

$$\begin{cases} x_2 = x_0, \\ y_2 = y_0 - 2 * M_2 \\ z_2 = z_0 - 2 * M_2 * \dfrac{p_0}{n_0} \end{cases} \tag{16}$$

$$L_{12} = L_{01} - 2 * (L_{01} \cdot n_B) n_B \tag{17}$$

$$L_2 = m[L_{12} - (L_{12} \cdot n_C) n_C] + \sqrt{1 - m^2 + m^2 (L_{12} \cdot n_C)^2} \cdot n_C \tag{18}$$

$$\theta_{out} = cos^{-1}(L_2 \cdot [0\ 0\ -1]) \tag{19}$$

Where p_0 and n_0 are the elements of the direction vector in y and z-axis in the Cartesian coordinate system.

4. Simulation results

4.1. Simulated time-shift signals

In the following simulations of the time-shift signal for an ellipsoidal droplet, the volume of the droplet has been kept constant at the volume of a 100 μm drop; the aspect ratio has been varied among the values η= 0.9, 1.0 and 1.1 and the relative refractive index has taken the values m = 1.33, 1.36 and 1.40.

In Figure 6, the left diagram presents the simulated time shift-signal for different relative refractive indexes and the right diagram shows the relationship between the exit angle of second-order refraction scattering and the corresponding incident angle, when the aspect ratio is 0.9 (Eq. (19)). The red dashed line and the green dashed line represent the upper and lower exit angle range for which reflective light will fall onto the detector. Only when the exit angle of the second-order refraction scattering is in the angle range between the green dashed line and red dashed line, will the exit ray be incident on the detector. When the refractive index is 1.33, the incident angle range for second-order refraction scattering results in two, well-separated regions for the incident angle, yielding also two well-separated peaks in the time-shift signal. These two peaks correspond to the p = 2.1 and 2.2 modes respectively. For the relative refractive index of 1.36 and 1.40 the incident angle for the p = 2.1 and 2.2 modes does not exhibit distinct ranges and the peaks in the time-shift signal for these modes overlap with each other, as seen in the left diagram of Figure 6.

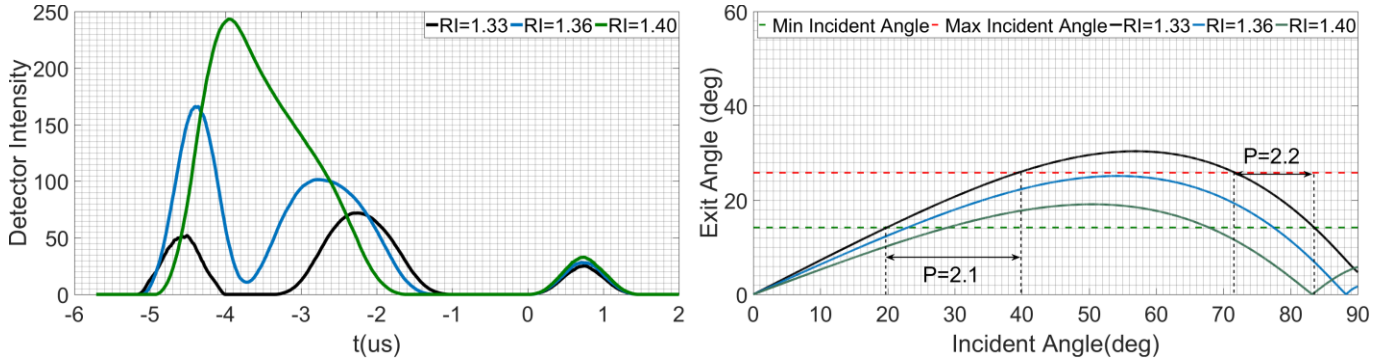

Figure 6: Left - simulated time-shift signal for different relative refractive indexes; Right - relationship between incident angle and exit angle of second-order refractive scattering, for an aspect ratio of 0.9. (RI stands for refractive index)

From Figure 7, computed for an aspect ratio of 1.0, the two signal peaks corresponding to second-order refractive scattering are distinct for all relative refractive indexes.

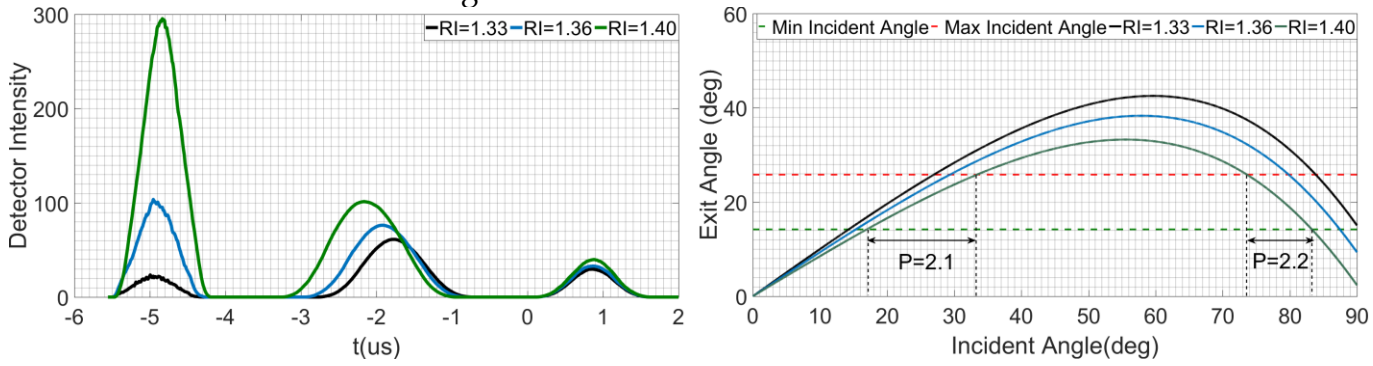

Figure 7: Left - simulated time-shift signal for different relative refractive indexes; Right - relationship between incident angle and exit angle of second-order refractive scattering, for an aspect ratio of 1.0. (RI stands for refractive index)

For the aspect ratio 1.1, shown in Figure 8, the incident angle range for the mode p = 2.2 and for the relative refractive indexes 1.40 is larger than the angle range for m = 1.36. For the relative refractive index 1.33, no angle range for mode p =2.2 exists, which means the time-shift signal for the mode p =2.2 does not exist and no respective peak appears in the signal (left diagram in Figure 8.

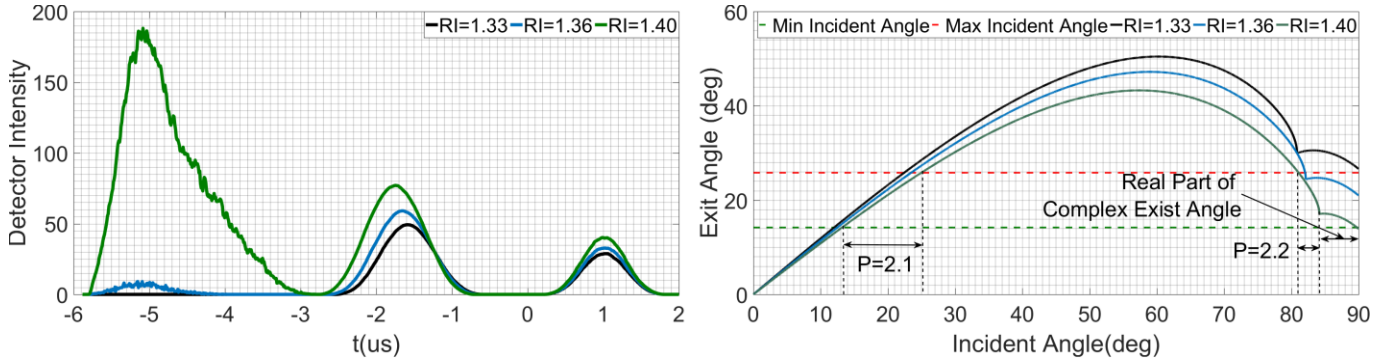

Figure 8: Left - simulated time-shift signal for different relative refractive indexes; Right - relationship between incident angle and exit angle of second-order refractive scattering, for an aspect ratio of 1.1. (RI stands for refractive index)

4.2. Evaluation of the ellipsoid particle size

For a typical time-shift signal, there are several ways to evaluate the particle size, as Figure 4 illustrates. The particle size has been calculated with various time differences by using Eqs. (20-21) derived in [20] and the evaluation results are tabulated in Table 1, as well as an average of the results from both evaluation methods.

$$d = \Delta t_{00} * \frac{v_z}{cos\frac{\theta_s}{2}} \tag{20}$$

$$d = \Delta t_{2121} * \frac{v_z}{sin\,\theta_i^{(p=2.1)}} \tag{21}$$

Aspect Ratio \ Rel. Refractive Index	1.33	1.36	1.40
b/a=0.9 *a*=51.787 μm *b*=46.609 μm *c*=51.787 μm	$d_{\Delta t_{00}} = 43.65\ \mu m$ $d_{\Delta t_{2121}} = 64.52\ \mu m$ $\frac{d_{\Delta t_{00}}+d_{\Delta t_{2121}}}{2}$=54.085 μm	$d_{\Delta t_{00}} = 40.77\ \mu m$ $d_{\Delta t_{2121}} = 74.09\ \mu m$ $\frac{d_{\Delta t_{00}}+d_{\Delta t_{2121}}}{2}$=57.43 μm	$d_{\Delta t_{00}} = 42.50\ \mu m$ Signal for second order refraction scattering P=2.2 with P=2.1 overlap with each other
b/a=1 *a*=50 μm *b*=50 μm *c*=50 μm	$d_{\Delta t_{00}} = 49.81\ \mu m$ $d_{\Delta t_{2121}} = 50.57\ \mu m$ $\frac{d_{\Delta t_{00}}+d_{\Delta t_{2121}}}{2}$=50.19 μm	$d_{\Delta t_{00}} = 49.81\ \mu m$ $d_{\Delta t_{2121}} = 50.73\ \mu m$ $\frac{d_{\Delta t_{00}}+d_{\Delta t_{2121}}}{2}$=50.27 μm	$d_{\Delta t_{00}} = 49.81\ \mu m$ $d_{\Delta t_{2121}} = 50.74\ \mu m$ $\frac{d_{\Delta t_{00}}+d_{\Delta t_{2121}}}{2}$=50.275 μm
b/a=1.1 *a*=48.436 μm *b*=53.28 μm *c*=48.436 μm	$d_{\Delta t_{00}} = 60.83\ \mu m$ $d_{\Delta t_{2121}} = 45.66\ \mu m$ $\frac{d_{\Delta t_{00}}+d_{\Delta t_{2121}}}{2}$=53.245 μm	$d_{\Delta t_{00}} = 59.10\ \mu m$ $d_{\Delta t_{2121}} = 44.31\ \mu m$ $\frac{d_{\Delta t_{00}}+d_{\Delta t_{2121}}}{2}$=51.705 μm	$d_{\Delta t_{00}} = 56.80\ \mu m$ $d_{\Delta t_{2121}} = 41.87\ \mu m$ $\frac{d_{\Delta t_{00}}+d_{\Delta t_{2121}}}{2}$=49.335 μm

Table 1: Evaluation of the size of an ellipsoidal particle by using the simulated time-shift signal.

5. Discussion and Conclusions

The results from Table 1 indicate that for spherical drops the time-shift technique yields good estimates of drop diameter independent of which time shift is used for computation. This fact can be exploited in two ways. First, size can be computed using the time difference from both reflection and second-order refraction and only if the two estimates agree within bounds, will the value be accepted; hence this is a spherical validation check. If the two values do not agree, this is an indication of non-sphericity. Second, if the drop is non-transparent or semi-transparent, such that signal peaks from second-order refraction are very weak, the size estimate from reflective scattering should be sufficient.

However, the simulations indicate also that the time-shift signal is significantly affected by changing either the relative refractive index or the aspect ratio of an ellipsoidal drop. Quite generally, the deviation of the drop size calculated by using the time difference from the reflection scattering order (Δt_{00}) exhibits a different sign compared with the deviation of the drop size calculated by using the time difference from second-order refractive scattering (Δt_{2121}). This holds for all values of relative refractive index and aspect ratio investigated. Which of the two methods results in a positive or negative deviation depends on the aspect ratio. For oblate drops (b/a<1.0) the reflective estimate (Δt_{00}) lies below the true value and for prolate drops (b/a>1.0) the estimate exceeds the true size. However, using a combination of both calculation methods, i.e. the average drop size, the simulation indicates that the size measurement is more robust against a change of the aspect ratio and the relative refractive index. For the present ranges of aspect ratio and relative refractive index investigated, the average diameter fell within 14% of the true volume equivalent diameter.

Notable is the fact that for high values of relative refractive index and prolate drops, a size estimate cannot be made using second-order refraction, since the signal peak for p = 2.2 is missing.

As outlined in the section 2, the computational procedure introduced in this study is capable of also treating ellipsoidal drops with arbitrary orientation with respect to the incident beam. The present results have focused only on cases in which the drop z-axis was aligned with the incident beam propagation direction. The next step in this study is to investigate the sensitivity of the time-shift technique to drop rotations.

6. Acknowledgements

The authors would like to thank the Federal Ministry for Economic Affairs and Energy of Germany for financial support through the Central Innovation Programme for SMEs (ZIM), contract ZF4415101LT7. They also appreciate the cooperation of the High-Performance

Computing Center of the TU Darmstadt. The authors are grateful for the very fruitful discussions with Professor Zhou Wu from University of Shanghai for Science and Technology.

References

[1] AOM-Systems, https://www.aom-systems.com/de/

[2] J.A. Arnaud, H. Kogelnik. Gaussian light beams with general astigmatism. Appl Opt, 8: 1687-1694, DOI: 10.1364/ AO.8.001687, 1969.

[3] C. Tropea. Optical particle characterization in flows. Annual Review of Fluid Mechanics, 43:399–426, 2011.

[4] C. Tropea, T.-H. Xu, F. Onofri, G. Gréhan, P. Haugen, and M. Stieglmeier. Dual-mode phase-Doppler anemometer. Particle & Particle Systems Characterization, 13(2):165–170, 1996.

[5] Debije (Debye) P. Das elektromagnetische Feld um einen Zylinder und die Theorie des Regenbogens, Physikalische Zeitschrift 9:775-778, 1908.

[6] D. L. Black, M. Q. McQuay, and M. P. Bonin. Laser-based techniques for particle-size measurement: a review of sizing methods and their industrial applications. Progress in Energy and Combustion Science, 22(3):267–306, 1996.

[7] D. R. Alexander, K. J. Wiles, S. A. Schaub, and M. P. Seeman. Effects of non-spherical drops on a phase Doppler spray analyzer. Particle Sizing and Spray Analysis, volume 573, pages 67–73. International Society for Optics and Photonics, 1985.

[8] E. Hecht. Optics, 4th. International Edition, Addison-Wesley, San Francisco, 2002.

[9] F. Xu, J. A. Lock, and C. Tropea. Debye series for light scattering by a spheroid. JOSA A, 27(4):671–686, 2010.

[10] G. Mie. Beiträge zur Optik trüber Medien, speziell kolloidaler Metallösungen. Annalen der Physik (4) 25:377.452, 1908.

[11] H.-E. Albrecht, N. Damaschke, M. Borys, and C. Tropea. Laser Doppler and Phase Doppler Measurement Techniques. Springer Science & Business Media, Heidelberg, 2013.

[12] H. Yu. Laser Beam Interaction with Spheroidal Droplets: Computation and Measurement. PhD thesis, tuprints, Technische Universitaet Darmstadt, 2013.

[13] H. Yu, F. Xu, and C. Tropea. Optical caustics associated with the primary rainbow of oblate droplets: simulation and application in non-sphericity measurement. Optics Express, 21(22):25761–25771, 2013.

[14] H. Yu, F. Xu, and C. Tropea. Spheroidal droplet measurements based on generalized rainbow patterns. Journal of Quantitative Spectroscopy and Radiative Transfer, 126:105–112, 2013.

[15] J. A. Lock and F. Xu. Optical caustics observed in light scattered by an oblate spheroid. Applied Optics, 49(8):1288– 1304, 2010.

[16] Kochkina. Stigmatic and Astigmatic Gaussian Beams in Fundamental Mode. Ph.D. thesis. Leibniz Universität Hannover, http://edok01.tib.uni-hannover.de/edoks/e01dh13/757170285.pdf, 2013.

[17] N. Damaschke, G. Gouesbet, G. Gréhan, H. Mignon, and C. Tropea. Response of phase Doppler anemometer systems to nonspherical droplets. Applied Optics, 37(10):1752–1761, 1998.

[18] P. G. Stegmann, C. Tropea, E. Järvinen, and M. Schnaiter. Comparison of measured and computed phase functions of individual tropospheric ice crystals. Journal of Quantitative Spectroscopy and Radiative Transfer, 178:379–389, 2016.

[19] B.E.A. Saleh, M.C. Teich. Fundamental of Photonics, 2nd ed. John Wiley & Sons, Inc, Hoboken, New Jersey, 2007.

[20] W. Schäfer and C. Tropea. Time-shift technique for simultaneous measurement of size, velocity, and relative refractive index of transparent droplets or particles in a flow. Applied Optics, 53(4):588–597, 2014.